The C-Terminal Transmembrane Domain of Bcl-x_L Mediates Changes in Mitochondrial Morphology

Jing-Yi Zheng,* Yien-Che Tsai,† Pradeep Kadimcherla,* Rong Zhang,‡ Julia Shi,§ George A. Oyler,¶ and Nada N. Boustany*

*Department of Biomedical Engineering, Rutgers University, Piscataway, New Jersey; †Laboratory of Protein Dynamics and Signaling, National Cancer Institute, Frederick, Maryland; ‡Department of Computer and Information Science and Engineering, University of Florida, Gainesville, Florida; §Department of Medicine, University of Maryland, Baltimore, Maryland; and ¶Department of Chemical and Biomolecular Engineering, Johns Hopkins University, Baltimore, Maryland

ABSTRACT We investigate the effect of mitochondrial localization and the Bcl-x_L C-terminal transmembrane (TM) domain on mitochondrial morphology and subcellular light scattering. CSM 14.1 cell lines stably expressed yellow fluorescent protein (YFP), YFP-Bcl-x_L, YFP-Bcl-x_L-ΔTM, containing the remainder of Bcl-x_L after deletion of the last 21 amino acids corresponding to the TM domain, or YFP-TM, consisting of YFP fused at its C-terminal to the last 21 amino acids of Bcl-x_L. YFP-Bcl-x_L and YFP-TM localized to the mitochondria. Their expression decreased the intensity ratio of wide-to-narrow angle forward scatter by subcellular organelles, and correlated with an increase in the proportion of mitochondria with an expanded matrix having greatly reduced intracristal spaces as observed by electron microscopy. Cells expressing YFP-TM also exhibited significant autophagy. In contrast, YFP-Bcl-x_L-ΔTM was diffusely distributed in the cells, and its expression did not alter light scattering or mitochondrial morphology compared with parental cells. Expression of YFP-Bcl-x_L or YFP-Bcl-x_L-ΔTM provided significant resistance to staurosporine-induced apoptosis. Surprisingly however, YFP-TM expression also conferred a moderate level of cell death resistance in response to staurosporine. Taken together, our results suggest the existence of a secondary Bcl-x_L function that is mediated by the transmembrane domain, alters mitochondrial morphology, and is distinct from BH3 domain sequestration.

INTRODUCTION

Proteins of the Bcl-2 family are important regulators of apoptosis, a highly controlled form of cell death fundamental to tissue development and homeostasis. Bcl-2 family members share Bcl-2 homology (BH) domains. The family includes multidomain pro-apoptotic proteins (e.g., Bax, Bak) containing BH1-BH3, multidomain anti-apoptotic proteins (e.g., Bcl-2, Bcl-x_L) containing all four BH1-BH4 domains, and ''BH3-only'' pro-apoptotic proteins (e.g., Bid, Bad, Bim, Noxa) containing only the BH3 domain. Multidomain Bcl-2 family proteins also possess a transmembrane (TM) C-terminal region, which can localize within organellar membranes including the outer membrane of the mitochondria. Bcl-2 family proteins can promote or inhibit apoptosis by regulating the release of pro-apoptotic factors, such as cytochrome *c*, Smac/Diablo, and Omi/Htra2, from the mitochondria. Once released into the cytoplasm, these factors activate caspases resulting in nuclear fragmentation and orderly dismantling of the cell (1,2).

The mechanisms of action of Bcl-2 proteins are not completely elucidated. Interaction between Bcl-2 family members is thought to involve the hydrophobic pocket formed by the close arrangement of the BH1-BH3 domains of a multidomain protein. This hydrophobic pocket can fit the exposed BH3 domain of another multidomain protein or of a BH3-only protein (3,4). In the case of Bax, the hydrophobic pocket can also sequester the C-terminal domain within the same monomer (5). Additionally, a possible interaction between the C-terminal of Bcl-x_L and the hydrophobic pocket of another Bcl-x_L or Bax protein forming either homodimers or heterodimers has been reported (6). Experimental evidence strongly suggests that pro-apoptotic Bax and Bak, are necessary for mitochondria-mediated apoptosis, and that their simultaneous deletion renders cells highly resistant to many apoptosis stimuli (7–9). Upon interaction with activated BH3-only proteins, Bax and Bak are triggered to oligomerize in the mitochondrial membrane forming pores, from which pro-apoptotic factors, such as cytochrome *c*, are released (10,11). Anti-apoptotic Bcl-2 family members can sequester BH3 proteins that would otherwise activate Bax and Bak (9), or they may directly interact with, and inhibit Bax or Bak (12–15). Interaction of BH3-only proteins with Bcl-2 and Bcl-x_L can also serve to displace Bax/Bcl-2 or Bak/Bcl-x_L binding, and therefore reactivate Bax and Bak (15).

While some Bcl-2 family homologs are initially located on the mitochondria (Bak, Bcl-2), others translocate from the cytosol to the mitochondria in response to a cell death stimulus (Bax, Bid) (1,2). Bcl-x_L is usually initially associated with mitochondria (16,17), but translocates in some cells from the cytoplasm to the mitochondria after an apoptosis stimulus (18,19). The localization of some Bcl-2 family proteins to the mitochondria seems obviously necessary to control directly the release of mitochondrial factors, such as

Submitted January 17, 2007, and accepted for publication August 7, 2007.

Address reprint requests to N. N. Boustany, PhD, Tel.: 732-445-4500, x6320; E-mail: nboustan@rci.rutgers.edu.

Editor: Michael Edidin.

© 2008 by the Biophysical Society

0006-3495/08/01/286/12 $2.00

doi: 10.1529/biophysj.107.104323

cytochrome *c*. Consistent with this, Bcl-2 family members can directly interact with the mitochondrion affecting both its structure and function. Mitochondrial localization of pro-apoptotic Bcl-2 family members has been associated with alterations in mitochondrial morphology and bioenergetics (20–25). At the same time, anti-apoptotic proteins, such as Bcl-2 and Bcl-x_L have been shown to preserve mitochondrial integrity, including membrane potential, outer membrane metabolite exchange, and osmotic integrity, in the face of cell death insults (25–31).

The mechanisms by which structural changes in the mitochondrial matrix and membranes may affect subsequent function have long been under study. Electron microscopy studies of mitochondria have shown that alterations in mitochondrial morphology are associated with different mitochondrial metabolic states (32–37). More recent electron tomography studies of mitochondria strongly suggest that specific compartmentation of the mitochondrial matrix may help localize respiration, and in the case of apoptosis help to free cytochrome *c*, and facilitate its release from the intermembrane space (20,38–41). As such, tracking changes in mitochondrial structure can provide a way to monitor mitochondrial function, and may provide important clues regarding the function of Bcl-2 family proteins in apoptosis at the level of the mitochondria.

Changes in the morphology of the mitochondrial matrix involve structural variation on the order of 10 to several hundred nanometers, and are typically assessed by electron microscopy (42). Electron microscopy is not easily amenable to study dynamic changes in mitochondrial structure within living cells or intact tissue. Thus, studies of isolated mitochondria (e.g., (34,37)), and of mitochondria within living cells (e.g., (43–46)), or in whole tissues (e.g., (47,48)), have relied on light scattering as a method to probe mitochondrial morphology without sample fixation or freezing. Light scattering does not provide the level of morphological detail achieved by electron microscopy. However, the technique can be invaluable for continuous monitoring of nanoscale morphological activity in situ, and ultimately discovering time points at which structural changes occur and can be further evaluated. Using this approach, we have found that the light scattering properties of apoptotic rat undifferentiated mesencephalic CSM 14.1 cells are altered after expression of Bcl-x_L fused to yellow fluorescent protein (YFP-Bcl-x_L) (49). Utilizing the expression of a Bcl-x_L mutant lacking the C-terminal TM domain (YFP-Bcl-xL-ΔTM), we further show in this study that the observed change in light scattering requires mitochondrial localization, and is accompanied by expansion of the mitochondrial matrix, as observed by electron microscopy. In addition we also show that expression of the Bcl-x_L C-terminal TM domain fused to YFP (YFP-TM), and lacking the rest of the Bcl-x_L protein, is by itself sufficient to alter mitochondrial morphology and confer a limited level of resistance to staurosporine-induced apoptosis.

METHODS

Gene constructs

Mouse BCL-x_L was previously cloned into the pEYFP-C1 vector (Clontech, BD Biosciences, Palo Alto, CA) using the *Bgl*II restriction site to yield a plasmid encoding an enhanced yellow fluorescent protein (YFP) fused to Bcl-x_L (49). YFP-BCL-x_L-ΔTM, consisting of the YFP coding sequence fused to BCL-x_L, from which the last 63 bases were truncated, was generated by polymerase chain reaction with BCL-x_L as template and the upper primer, 5′-GGACTCAGATCTATGTCTCAGAGCAACCGGGAG-3′, and lower primer 5′-CTGCAGAATTCTCAGCGGTTGAAGCGTTCCTGGCC-3′. BCL-x_L-ΔTM was subcloned into the pEYFP-C1 vector at the *Bgl*II/*Eco*RI sites. The sequence of the final product matched BCL-x_L in the GenBank database. Compared to the reference sequence, and in addition to the C-terminal truncation, our sequence contained a C209G mutation, leading to a glycine (GGC) instead of an alanine (GCG) at amino acid No. 70 in the Bcl-x_L protein. The same mutation was reported in one other BCL-x_L Beta sequence listed in the public database.

YFP-TM, consisting of the YFP coding sequence fused to the last 63 bases of the BCL-x_L gene, was generated by polymerase chain reaction with pEYFP-C1 as template and the upper primer, 5′-AGATCCGCTAGCGCTACCGGTCGCCACCATGGTGAGC-3′ and lower primer 5′-CGACTGCAGAATTCATTTCCGACTGAAGAGTGAGCCCAGCAGAACCACGCCGGCCACAGTCATGCCCGTCAGGAACCAAGATCTGGATCC-3′ (TM sequence underlined). YFP-TM was subcloned into the pECFP-C1 vector (Clontech) replacing the CFP sequence between the *Nhe*I and *Eco*R1 sites. The sequence of the final amplified and purified product after cloning into the pECFP-C1 vector confirmed the presence of 5′-YFP-TCCGGACTCAGATCT-TM-TGA. The sequence between YFP and TM is the same as the beginning of the multiple cloning site in the pEYFP-C1 vector.

Generation of stable cell-lines

Stable expression of YFP, and YFP-BCL-x_L in inducible, rat mesencephalic CSM14.1 cells was described previously (49). In this study, CSM 14.1 cells were transfected at 80–90% confluence with an empty plasmid encoding hygromycin resistance (pIREShyg3, Clontech) and either YFP-BCL-x_L-ΔTM or YFP-TM (1:10 molar ratio, hygromycin plasmid: fluorescent protein plasmid) using lipofectamine 2000 in OptiMEM medium (Invitrogen, Rockville MD). Immortalized baby mouse kidney (iBMK) cells were transfected at 80–90% confluence with YFP-BCL-x_L, YFP-BCL-x_L-ΔTM, YFP-TM, or YFP. Twenty-four hours posttransfection, the cells were subcultured at 1000 cells/78.5 cm^2 (10 cm dish) in growth medium supplemented with 400 μg/ml hygromycin B (Invitrogen) for CSM14.1 selection, or 1 mg/ml geneticin sulfate (G418; Invitrogen) for iBMK selection. Isolated foci with yellow fluorescence were picked, serially diluted, and replated in 96-well plates to obtain clonal cell-lines. In CSM14.1 cells, expression of YFP constructs was confirmed by immunoblots and fluorescence microscopy; in iBMK cells, by fluorescence microscopy.

Cell culture

CSM 14.1 cell lines were maintained in Dulbecco's modified Eagle's medium (DMEM) supplemented with 10% (V:V) fetal bovine serum (FBS), 1% (V:V, ~0.1 mM) nonessential amino acid, 100 Units/ml penicillin, 100 μg/ml streptomycin, and 1 mg/ml geneticin sulfate (G418). DMEM (catalog No. 11965092), FBS, nonessential amino acids, penicillin, and streptomycin were from Invitrogen. CSM 14.1 cells were kept undifferentiated in culture at 32°C in a 5% CO_2 in air atmosphere. Stable CSM 14.1 cell-lines transfected in this study with YFP-BCL-xL-ΔTM and YFP-TM were maintained in the growth medium described above supplemented with 400 μg/ml hygromycin B. iBMK cells were maintained at 38°C in a 5% CO_2 in air atmosphere in DMEM supplemented with 10% (V:V) FBS (Gemini Bio-Products, West Sacramento, CA), and 100 Units/ml penicillin, 100 μg/ml

streptomycin. For microscopy, cells were cultured on glass coverslips, which, only in the case of CSM 14.1 cells, were coated with poly-D lysine (MW > 300,000; Sigma Chemical, St. Louis, MO).

Immunoblots

CSM 14.1 cells were washed with phosphate buffered saline (PBS), and lysed in SDS buffer (10 mM HEPES pH7.4, 38 mM NaCl, 2% sodium dodecyl sulfate) supplemented with 1 μg/ml leupeptin, 1 μg/ml aprotinin, and 0.2 mM phenylmethylsulfonyl fluoride. Leupeptin, aptotinin, and phenylmethylsulfonyl fluoride were from Sigma Chemical. The lysates' protein content was determined by a colorimetric bicinchoninic acid analysis (BCA; Pierce, Rockford, IL). For each cell variant, 30 μg of cell lysate protein were resolved by 12% standard sodium dodecyl sulfate-polyacrylamide gel electrophoresis. After transfer to a polyvinylidene difluoride membrane by semidry electroblotter (Bio-Rad, Hercules, CA), blots were blocked with 5% milk with 0.05% Tween-20 in TBS buffer (20 mM Tris, 500 mM NaCl, pH 7.5), incubated with mouse anti-GFP antibody (0.2 μg/ml, GFP-B-2, catalog No. SC-9996; Santa Cruz Biotechnology, Santa Cruz, CA) followed by incubation with peroxidase conjugated goat anti-mouse IgG (0.2 μg/ml, Chemicon International No. AP308P), and developed with enhanced chemiluminescence reagents (Amersham, Piscataway, NJ).

Fluorescence microscopy

YFP fluorescence was imaged using a YFP filter cube (filter No. 46; Carl Zeiss, Göttingen, Germany): excitation, 500 ± 20 nm bandpass; emission, 515 nm dichroic mirror followed by a 535 ± 30 nm bandpass filter. Mitochondria were also specifically imaged by immunofluorescence of the complex V unit. For this, cells were grown on glass coverslips to ~70% confluence, washed with PBS, and fixed for 1 min in a 1:1 V:V, methanol/acetone solution, which had been stored at −20°C. After three washes in PBS, samples were incubated at 37°C for 1 h in blocking buffer (2% fetal bovine serum in PBS) followed by 1 h in blocking buffer supplemented with 2 μg/ml anti-OxPhos complex V subunit α-mouse IgG2b (A21350, Invitrogen). The samples were washed in PBS and further incubated at 37°C for 1 h in blocking buffer supplemented with 1.5 μg/ml Tetramethylrhodamine goat anti-mouse IgG (T2762, Invitrogen). Coverslips were finally washed three times with PBS and mounted on microscope slides with SlowFade (S2828; Invitrogen). For the YFP CSM 14.1 cell variant, fixation and immunofluorescence labeling were done at room temperature, immediately after imaging YFP fluorescence. Rhodamine fluorescence was detected with a standard rhodamine filter cube (filter No. 20; Carl Zeiss): excitation, 546 ± 12 nm bandpass; emission, 560 nm dichroic mirror followed by a 575–640 nm band pass filter. For the same image acquisition time in each channel, the equivalent of 3.36% of rhodamine signal measured in the rhodamine channel spilled over into the YFP channel, while the equivalent of 3.44% of YFP signal measured in the YFP channel spilled over into the rhodamine channel. Fluorescence images of samples double-labeled with YFP and anti-Complex-V/rhodamine were corrected for this spillover.

Optical scatter microscopy

The optical scatter imaging technique was described previously in detail (44,50). In this study, the specimens were mounted on the stage of an inverted light microscope (Axiovert 200M; Carl Zeiss), with epifluorescence and differential interference contrast (DIC) capabilities. The condenser was adjusted to central Köhler illumination with a numerical aperture (NA) of 0.05 (condenser front aperture closed). A 10-nm bandpass interference filter (Thorlabs, Newton, NJ) placed in the condenser housing yielded an incident red beam centered at $\lambda = 630$ nm. The images were collected with a 63× oil immersion objective, NA = 1.4, and displayed on a charge-coupled device camera (Cascade 512B, Roper Scientific, Tucson, AZ). In a Fourier plane conjugate to the back focal plane of the objective, a beam stop, diameter = 0.7 mm, was placed in the center of an iris with variable diameter. The beam stop blocked the unscattered transmitted light through the sample, while the variable iris diameter was switched between low NA and high NA positions, collecting light scattered within a solid angle bound by $3° < \theta < 10°$ and $3° < \theta < 67°$, respectively.

Optical scatter image acquisition and analysis

Each coverslip with attached live cells was mounted by means of a steel plate onto the stage of the inverted microscope. Just before mounting onto the microscope's stage, the DMEM growth medium was replaced with Leibovitz L15 medium (Invitrogen) supplemented with 10% fetal bovine serum, 100 Units/ml penicillin, and 100 μg/ml streptomycin. The cells were monitored by DIC, fluorescence, and optical scatter microscopy at room temperature and room air. For optical scatter imaging, two sequential dark-field images of each cell sample were acquired at high and low NA by manually switching the diameter of the variable iris. A sample of L15 growth medium was used to collect background scatter signal due to the microscope optics. Dividing the background-subtracted high NA images by their corresponding background subtracted low NA images resulted in ratiometric optical scatter images, which directly encode the high-to-low NA optical scatter image ratio (OSIR) at each pixel in the field of view. The OSIR corresponds to the intensity ratio of wide-to-narrow angle forward scatter defined as

$$OSIR = \frac{\int_{\varphi=0°}^{360°}\int_{\theta=3°}^{67°} F(\theta,\varphi)\sin\theta d\theta d\varphi}{\int_{\varphi=0°}^{360°}\int_{\theta=3°}^{10°} F(\theta,\varphi)\sin\theta d\theta d\varphi}, \quad (1)$$

where $F(\theta,\varphi)$ gives the intensity of the light scattered in a given direction defined by the angles θ and φ. The value θ is the angle between the scatter direction and the direction of propagation of the incident light, and φ is the azimuthal angle of scatter.

Optical scatter images were acquired in IPlab (BD Biosciences Bioimaging, Rockville, MD) and processed in MatLab (The MathWorks, Natick, MA). In each experiment, a segment was manually defined around every cell in the DIC images. These segments were overlaid onto the optical scatter images such that data analysis was limited to regions containing a cell. Only positively fluorescent cells were analyzed in the transfected cell variants. In addition, we further segmented the regions in the YFP-TM cells that corresponded to bright and punctate fluorescent mitochondria (see also Results) to measure the OSIR at these specific locations. Two criteria were used to locate these small bright regions in the YFP-TM fluorescence images. First, each of these regions was centered on a local maximum of the intensity profile. These local maxima were detected using a two-dimensional order-statistic filter (51). Second, local maxima with intensity above background were selected. Since the YFP-TM fluorescence images did not have uniform exposure, setting a single threshold was not possible. Instead, a Laplacian filter (52) was used to measure the second spatial derivative in the image, and only retrieve peaks with large intensity changes. At completion of the algorithm, we verified that the detected local peaks corresponded to the punctate mitochondria in the fluorescence images.

Cell death assay

Cell death resistance was assayed by measuring the percentage of dead cells in response to staurosporine (STS) treatment. Cells were cultured in 12-well plates, and treated with 1 μM STS (Sigma Chemical) at 90% confluence. After 24 h, 40 μM propidium iodide (Invitrogen) was added to the incubated cultures for 15 min. The cells were collected from the plates by pipetting and trituration. Microscopic observation of the plates insured that all cells were collected by this process. The cell suspension was concentrated to $\sim 5 \times 10^5$ cells/ml by centrifugation and partial removal of the supernatant. The number of cells with positive propidium iodide fluorescence in the final cell suspension was counted in a hemacytometer, and was taken to represent dead cells, which had lost membrane integrity. Propidium iodide fluorescence was visualized with the rhodamine filter cube described above (filter No. 20, Carl Zeiss).

Electron microscopy and mitochondrial counting

CSM 14.1 cells were grown to ~90% confluence in Sonic Seal Slide wells (No. 70365-42; Electron Microscopy Sciences, Hatfield, PA). The cells were washed (2×1 min) in PBS, and incubated for 2 h in Karnovsky's modified fixative (2.5% glutaraldehyde, 4% paraformaldehyde, 0.1 M sodium cacodylate, 8 mM calcium chloride, pH = 7.4; Electron Microscopy Sciences). After 2 h, the fixative was removed and replaced with another fresh aliquot of the same. Directly after this fixation, or after storage overnight at 4°C, the cells were washed (2×10 min) in cacodylate buffer (0.1 M sodium cacodylate, pH = 7.4), postfixed for 1 h at room temperature in cacodylate buffer supplemented with 1% osmium tetroxide, dehydrated in a graded series of acetone, and embedded in Epon-Spurr resin. Sections 90-nm-thin were cut on a model No. EM UC6 ultramicrotome (Leica Microsystems, Bannockburn, IL). Sectioned grids were stained with a saturated solution of uranyl acetate and lead citrate, and observed at 80 kV on a JEOL 1200EX transmission electron microscope (JEOL, West Chester, PA).

The electron micrographs revealed two types of mitochondria:

1. Mitochondria with a condensed matrix, which had visible cristae under 40,000× magnification.
2. Mitochondria with an ''expanded'' matrix, in which the intracristal spaces were greatly reduced and the cristae were not visible under up to 50,000× magnification.

The two types of mitochondria were counted at 40,000× in several arbitrary fields. The number of fields, and therefore the total area spanned, in each of the cell variants was the same. Approximately 150 mitochondria were counted per sample, and the count generally spanned between 15 and 20 cells. Mitochondria with a matrix, which seemed partially expanded and partially condensed, were taken as having a condensed matrix.

RESULTS

Expression of protein constructs in CSM 14.1 cells

To investigate the effect of Bcl-x_L localization on mitochondrial morphology, we generated four stable CSM 14.1 cell lines expressing YFP, YFP-Bcl-x_L, YFP-Bcl-ΔTM, or YFP-TM (Fig. 1 *A*). YFP-Bcl-x_L-ΔTM, consisted of YFP fused to Bcl-x_L lacking the last 21 amino acids at its C-terminal; YFP-TM of YFP fused to the last 21 amino acids Bcl-x_L. These 21 amino acids, WFLTGMTVAGVVLLGSLFSRK, constitute the C-terminal hydrophobic TM domain of Bcl-x_L (16). YFP expression and subcellular localization were confirmed by immunoblots against YFP, and fluorescence microscopy, respectively (Fig. 1, *B* and *C*). Cells expressing YFP-Bcl-x_L and YFP-Bcl-x_L-ΔTM exhibited a band at ~50 kDa corresponding to expression of the fusion construct YFP-Bcl-x_L. Cells transfected only with YFP or YFP-TM, and lacking Bcl-x_L, exhibited a band between 29 and 37 kDa corresponding to YFP expression. Cells expressing YFP-Bcl-x_L exhibited a filamentous yellow-green fluorescence distribution, which coincided with the distribution of the mitochondria assessed by immunofluorescence labeling of the ATP synthase (anti-OxPhos Complex V). When the TM domain of Bcl-x_L was deleted, the YFP-Bcl-x_L-ΔTM protein was diffusely distributed in the cells. In contrast, YFP fused to the TM domain (YFP-TM) specifically targeted the mitochondria. In >50% of the YFP-TM cells, we also found very round and bright punctate mitochondria (*arrows* in *last panel pair* of Fig. 1 *C*). Using fluorescence images, which were corrected for spillover between the YFP and Complex V rhodamine fluorescence channels, we normalized the YFP signal per pixel to the Complex V signal per pixel. Within a given cell, the normalized YFP-TM signal in these bright punctate mitochondria was typically approximately four times higher than the normalized YFP-TM signal in their long and filamentous counterparts.

Effect of Bcl-x_L and Bcl-x_L mutants on light scattering by CSM 14.1 cells

Representative optical scatter images are shown alongside DIC images for the CSM14.1 cell variants (Fig. 2 *A*). In the optical scatter images, the pixels directly encode the local value of the OSIR, which corresponds to the intensity ratio of wide-to-narrow angle forward scatter (Eq. 1). Note that the image pixel values correspond to OSIR × 100. For spheres with diameter between 0.015 μm and 2.72 μm, and with refractive index ratio $m = 1.04$, the calculated OSIR, based on Mie theory, decreases nonlinearly and monotonically from 33.65 to 1.15 as a function of diameter (Fig. 2 *B*). The OSIR was utilized as a measure of subcellular morphological change caused by expression of Bcl-x_L or its mutants. Cell by cell analysis showed that the mean OSIR per cell was decreased from 2.22 for parental cells to 1.80 for YFP-Bcl-x_L, and 1.97 for YFP-TM cells. The difference between the OSIR values of YFP-Bcl-x_L and parental cells, and YFP-TM and parental cells were significant with $p < 10^{-14}$ by Student *t*-test. In contrast, the mean OSIR per cell for Bcl-x_L-ΔTM was 2.23, and similar ($p = 0.78$) to that of the parental cells (Fig. 2 *C*), while the mean OSIR value of the YFP cells, 2.44, was 10% higher than that of the untransfected cells ($p < 10^{-3}$).

OSIR was binned into 326 elements with 0.1 intervals spanning 1.15–33.65. Pixel histograms were normalized to the number of pixels with OSIR = 1.15, and are displayed in the OSIR range 1.15–12.00, which included >95% of the pixels (Fig. 3 *A*). The unnormalized histogram means, which represent the ensemble of pixel values collected within a given variant, largely corroborate the single cell analysis. In particular, the mean pixel value was 18% lower for YFP-Bcl-x_L and 12% lower for YFP-TM compared with untransfected parental cells. The mean pixel value of the Bcl-x_L-ΔTM cells was similar to that of the parental cells (Fig. 3 *B*). However, the increase in the mean pixel value for YFP was only 1.3% by this analysis.

The YFP-TM histogram had a larger relative contribution from pixels with values above 200 compared with the YFP-Bcl-x_L histogram. To find out whether this difference in the YFP-TM histogram could be accounted for by the presence of the bright and punctate mitochondria found by fluorescence (Fig. 1 *C*), we specifically segmented out these bright regions in the YFP-TM fluorescence images and obtained a pixel histogram of the OSIR values falling specifically on

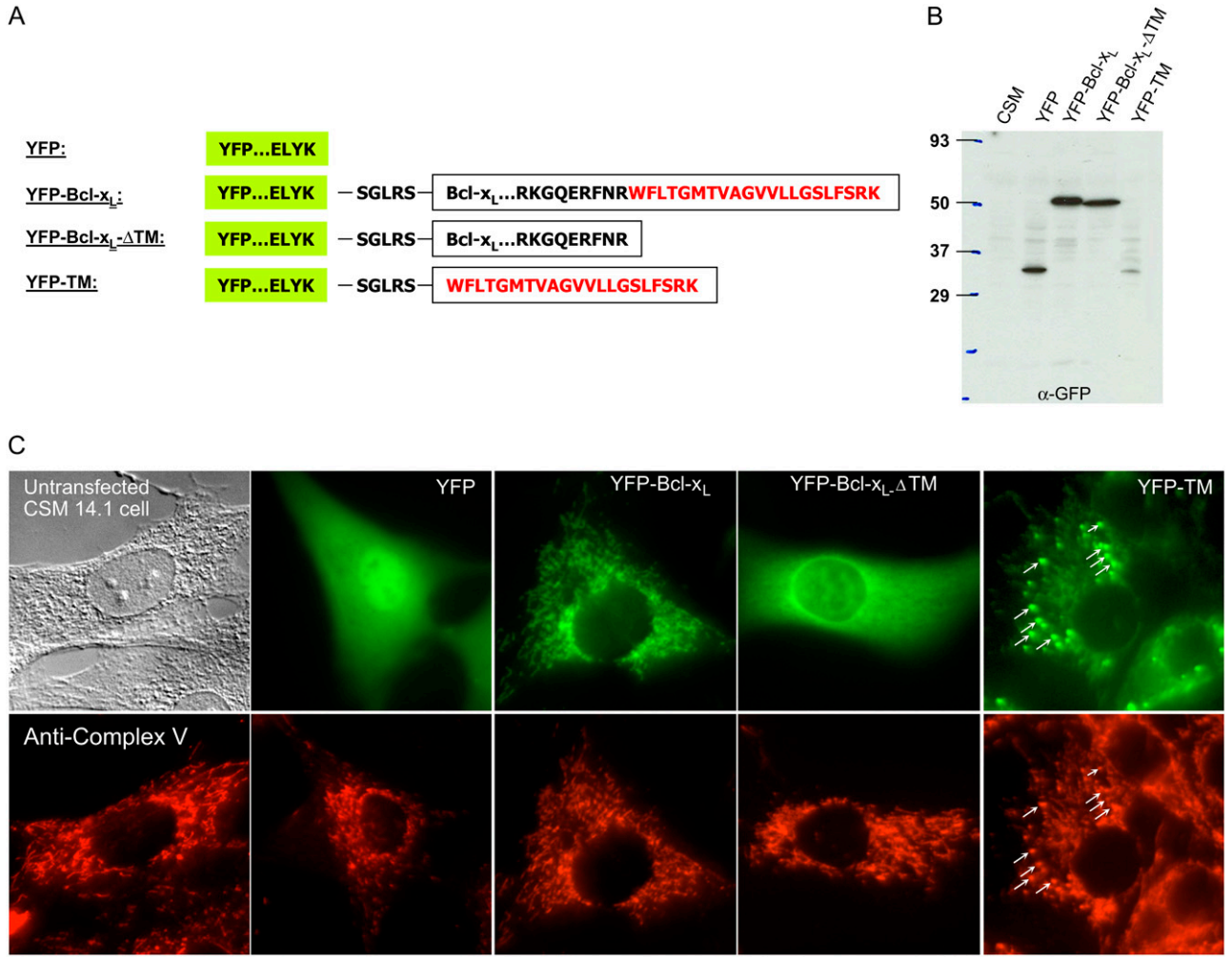

FIGURE 1 YFP constructs, YFP expression, and YFP localization in CSM 14.1 cell lines. (*A*) Bcl-x_L, Bcl-x_L-ΔTM, which lacks the last 21 amino acids of wild-type Bcl-x_L, or TM, which consists of the last 21 amino acids of Bcl-x_L, was fused to YFP. (*B*) YFP expression in CSM 14.1 cells was confirmed by Western blotting. As expected, a band between 29 and 37 kDa was found for cells transfected with YFP or YFP-TM. A band just above 50 kDa corresponds to the presence of YFP-Bcl-x_L and YFP-Bcl-x_L-ΔTM (Bcl-x_L is ~26 kDa). (*C*) Differential interference contrast (*upper left panel*) and fluorescent images of representative cells transfected with YFP, YFP-BCL-x_L, YFP-BCL-x_L-ΔTM, and YFP-TM. The distribution of YFP-Bcl-x_L and YFP-TM (*third* and *last panel pairs*) coincides with the distribution of mitochondria labeled with anti-OxPhos Complex V antibody. Very bright and punctate mitochondria were also found in >50% of the YFP-TM transfected cells (*arrows* in *last panel pair*). YFP distribution is diffuse in cells transfected with YFP and YFP-BCL-x_L-ΔTM.

these image segments. This histogram (line with *connected small squares* in Fig. 3 *A*) did not coincide with the YFP-TM histogram, and the pixel values associated with the bright and punctate mitochondria had an even larger proportion of pixels with values >200. The segments associated with the bright and round mitochondria represented only ~2% of all the pixels analyzed in the YFP-TM case. Thus, their histogram could not fully account for the shift in the YFP-TM histogram above the YFP-Bcl-x_L histogram.

Effect of Bcl-x_L and Bcl-x_L mutants on mitochondrial morphology

Alterations in subcellular morphology underlie changes in light scattering. Thus to corroborate the scattering data, and better characterize the morphological changes at hand, we used electron microscopy to image the cell variants. Since our YFP constructs were designed based on their mitochondrial targeting properties, we specifically looked for alterations in mitochondrial morphology. We identified two types of mitochondria in the CSM 14.1 cell variants:

1. Mitochondria with a condensed matrix, in which the cristae are clearly visible at 40,000× (Fig. 4, *black arrows*).
2. Mitochondria with an ''expanded'' matrix, in which the intracristal spaces were so reduced, the cristae could not be discerned under 40,000× or 50,000× (Fig. 4, *white arrows*).

By counting the number of each type of mitochondria in the cell variants considered, we found that cells expressing

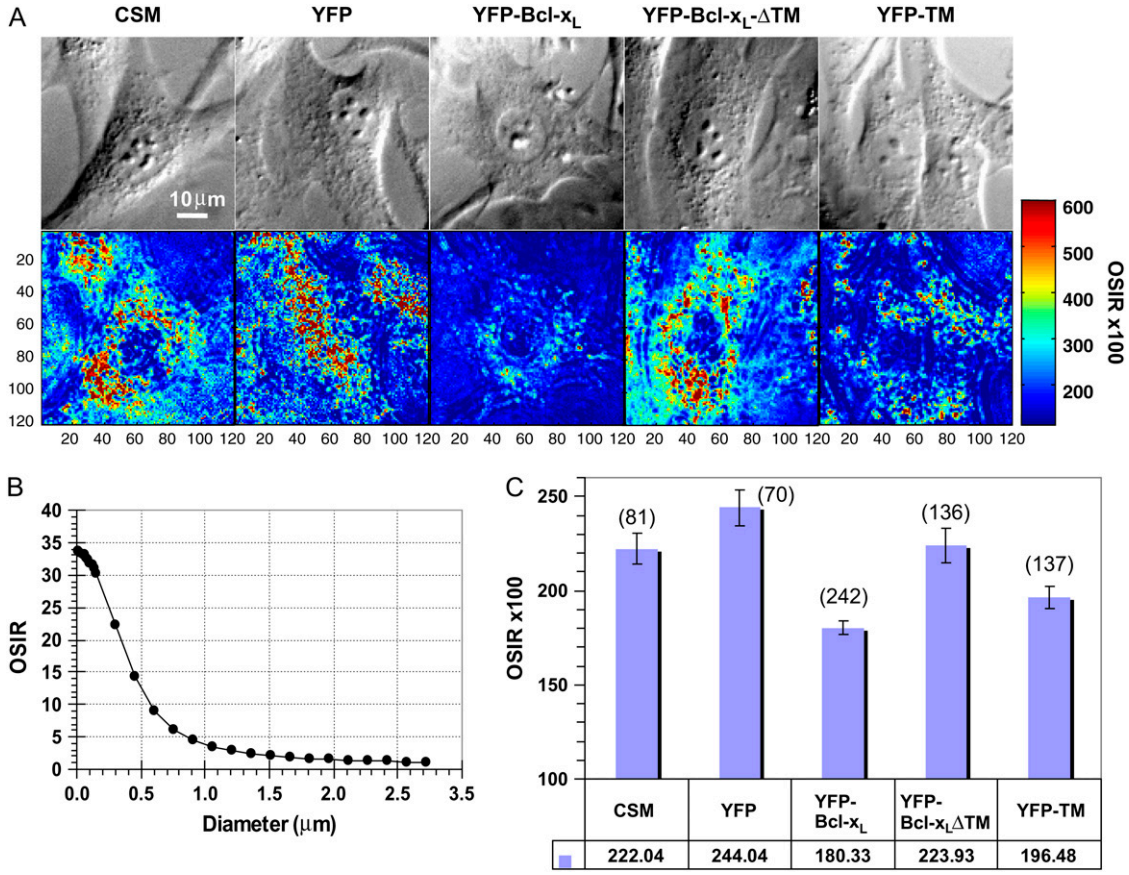

FIGURE 2 Optical scatter images (OSI) and optical scatter image ratio (OSIR) values in the CSM 14.1 cell variants. (*A*) Differential interference contrast (DIC, *top panels*), and OSI images of untransfected (*CSM*, *leftmost panels*) and transfected CSM 14.1 cells. OSI pixel values (*color bar*) encode local measurements of OSIR, which can be theoretically described by Eq. 1. Note that the image pixels encode OSIR × 100. (*B*) Mie theory prediction of the average OSIR per pixel expected from images of homogeneous suspensions of spheres with a given diameter. For spheres, the OSIR is expected to decrease monotonically with increasing sphere diameter D, for $0.015\ \mu m < D < 2.75\ \mu m$. (*C*) Mean OSIR per cell for each of the five CSM 14.1 cell variants. Error bars represent the 95% confidence interval of the mean, and the number in parenthesis is the number of cells tested.

YFP-Bcl-x_L or YFP-TM have a significantly higher proportion of mitochondria with expanded matrix (~70%), in contrast with untransfected cells (CSM), cells expressing YFP, or cells expressing YFP-Bcl-x_L-ΔTM, in which the proportion of mitochondria with condensed matrix was significantly higher (Fig. 5).

In addition, we found that unlike all other variants, a large number of YFP-TM cells showed evidence of autophagy (Fig. 6). In particular, out of ~50 cells, 80% of the YFP-TM cells had more than 20 autophagocytic vesicles, while <15% of the cells had >20 autophagic vesicles in the other variants. Moreover, all YFP-TM cells observed under electron microscopy had at least one such vesicle, while many cells in the other variants had none.

Effect of Bcl-x_L and Bcl-x_L mutants on apoptosis resistance

To study the potential relationship between mitochondrial morphology alterations and apoptosis resistance, we tested the effect of Bcl-x_L and Bcl-x_L mutants on cell death in response to staurosporine. Both CSM 14.1 and iBMK cells, which were tested in this part of the study, were previously shown to undergo apoptosis in response to staurosporine (49,53). After 24 h of treatment with 1 μM staurosporine, the percentage of dead cells was 31.7 ± 10.3% and 42.1 ± 6.3% for parental CSM 14.1 cells, and cells expressing YFP, respectively (Fig. 7). As expected, CSM 14.1 cells overexpressing Bcl-x_L were resistant to cell death and had only 2.3 ± 0.7% dead cells under the same treatment. YFP-Bcl-x_L-ΔTM induced as much cell death resistance as Bcl-x_L, 7.2 ± 5% dead cells. Surprisingly, in response to 24 h of STS treatment, CSM 14.1 cells also exhibited a moderate level of cell death resistance after YFP-TM transfection, 16.3% ± 5 dead cells, compared to 42.1 ± 6.3 dead cells for YFP. To test the reproducibility of these data in another cell line, we repeated our cell death resistance experiments in iBMK cells stably transfected with the same YFP constructs. The iBMK experiments corroborated the CSM 14.1 results. In both cases, Bcl-x_L-ΔTM conferred a strong level of resistance similar to

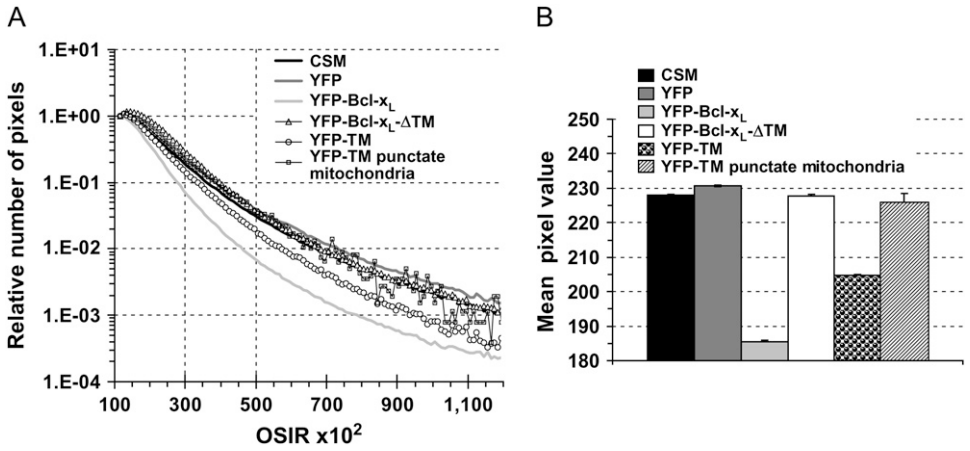

FIGURE 3 Pixel analysis of OSI images. (*A*) Pixel histograms normalized to the number of pixels with OSIR = 1.15 for the untransfected CSM 14.1 cells (*black*) and transfected CSM 14.1 variants (*dark gray*, YFP; *light gray*, YFP-Bcl-x_L; *triangles*, YFP-Bcl-x_L-ΔTM; *circles*, YFP-TM). Each histogram includes pixels from all the segmented cell images considered within a given variant. The line with connected small squares corresponds to the pixel histogram of the bright and punctate mitochondria, which were found by fluorescence in YFP-TM cells (see also *last panel pair* in Fig. 1 *C*) and segmented via a local intensity peak detection algorithm. (*B*) Mean of the unnormalized pixel histograms for each of the CSM 14.1 cell variants, and punctate mitochondria found in the YFP-TM cells. The error bar corresponds to the 95% confidence interval of the histogram mean.

that of Bcl-x_L, and YFP-TM provided a moderate level of resistance.

DISCUSSION

We had previously observed that expression of YFP-Bcl-x_L is specifically localized on the mitochondria, and alters angular light scattering by CSM 14.1 cells (49). By measuring the intensity ratio of wide-to-narrow angle scatter, OSIR, we had found a decrease in OSIR in response to YFP-Bcl-x_L expression. In this study, we report that this optical scatter change correlates with a high incidence of mitochondria with an expanded matrix, in which the intracristal spaces were so reduced they seemed absent as observed by electron microscopy at high magnification. Approximately 70% of mitochondria exhibited an expanded matrix in cells expressing YFP-Bcl-x_L, compared with only 30% of mitochondria with an expanded matrix in parental cells, or cells expressing only YFP. The relative OSIR values reported in this manuscript reproduce our earlier data for untransfected, YFP and YFP-Bcl-x_L CSM 14.1 cells (49). In both studies we found a ~20% OSIR decrease for YFP-Bcl-x_L, and a ~5–10% OSIR increase for YFP, compared with untransfected cells. The OSIR increase in YFP cells could not account for the decrease in OSIR observed in response to YFP-Bcl-x_L nor was it accompanied by alterations in mitochondrial morphology in this study. Whether YFP alters other scatterers in the cytoplasm remains to be evaluated.

To investigate the role of the Bcl-x_L TM domain and mitochondrial localization in mediating the observed optical scatter response and changes in mitochondrial morphology, we used a YFP-Bcl-x_L-ΔTM protein construct, in which Bcl-x_L lacks its last 21 amino acids corresponding to the C-terminal TM domain. In contrast to YFP-Bcl-x_L, expression of YFP-Bcl-x_L-ΔTM was diffuse within the cells, did not localize specifically on the mitochondria, did not alter light scattering, and was not accompanied by an increase in the percentage of mitochondria with an expanded matrix. These results show that alterations in light scattering and mitochondrial morphology that are induced by expression of YFP-Bcl-x_L, require the C-terminal TM domain and localization of YFP-Bcl-x_L on the mitochondria.

To find out whether the BH domains of Bcl-x_L are necessary to induce the observed mitochondrial alterations, we synthesized a YFP-TM construct consisting of eYFP fused to the last 21 amino acids of Bcl-x_L, without the rest of the Bcl-x_L protein. As expected, this construct targeted the mitochondria. In addition, like YFP-Bcl-x_L cells, cells expressing YFP-TM had a lower OSIR value and a larger proportion of mitochondria with an expanded matrix. Thus, the BH

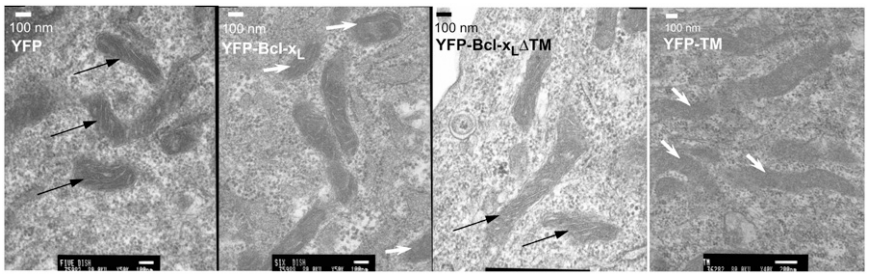

FIGURE 4 Representative electron micrographs of mitochondria with a condensed matrix (*black arrows*) or an expanded matrix (*white arrows*) found in the transfected CSM 14.1 cell variants. Mitochondria with a condensed matrix were ones in which at least one crista could be discerned, while mitochondria with an expanded matrix had very reduced intracristal spaces, such that no cristae could be discerned under up to 50,000× magnification.

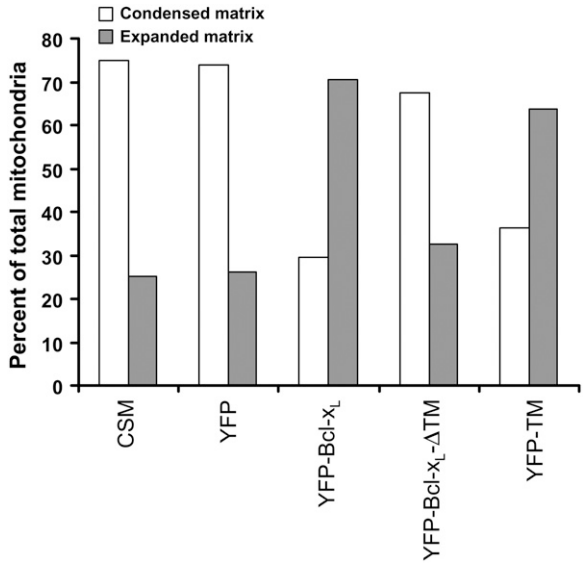

FIGURE 5 Proportion of observed mitochondria with expanded or condensed matrix within each cell variant.

domains of Bcl-x_L are not required, and the TM domain is sufficient to elicit changes in mitochondrial matrix morphology. However, unlike Bcl-x_L, a significant portion of the YFP-TM cells also exhibited a very large number of vesicles, suggestive of excessive autophagy. At the same time, >50% of the YFP-TM cells were found to contain very bright and punctate mitochondria observed by fluorescence (Fig. 1 *C*, *last panel pair*) and with a larger proportion of pixels with high OSIR values compared with the bulk of the YFP-TM cells (Fig. 3). By normalizing the YFP fluorescence to that of anti-complex V fluorescence, we found that the fluorescence intensity of the punctate mitochondria is greater than the fluorescence of filamentous looking mitochondria within the same cell. It is therefore conceivable that excessive YFP-TM expression on these punctate mitochondria may have targeted them for autophagy. A direct correlation between light and electron microscopy will be required to confirm whether the autophagocytic vesicles are indeed the result of mitochondrial autophagy, and if they correspond to the bright and punctate mitochondria observed by fluorescence. Kaufman et al. had reported that mitochondrial targeting requires two basic amino acids flanking the TM domain at each end (17). While in our construct, the TM domain was not explicitly preceded by the x-domain of Bcl-x_L (17), it did include two basic amino acids at each end (Fig. 1 *A*): . . .K. . .R on the YFP end, where K is part of the YFP terminus, and RK at the other end, coming from the original C-terminal of Bcl-x_L. This is consistent with the fact that fluorescence of our YFP-TM construct colocalized with anti-complex V fluorescence, and therefore was not simply a result of subcellular YFP-TM aggregation without specific localization to the mitochondria. The fact that YFP-TM, and not YFP-Bcl-x_L, should elicit an excessive autophagocytic response, remains to be determined but could be related to the interaction between Bcl-x_L and the recently discovered BH3 domain in Beclin1 (54,55). As such, YFP-TM, which lacks the hydrophobic cleft of Bcl-x_L, may be unable to bind Beclin1 and maintain a baseline inhibition of autophagy.

Finally, to investigate the role of the TM domain in apoptosis resistance, we measured the amount of cell death after 24 h of staurosporine treatment, which was previously shown to induce apoptosis in CSM 14.1 and iBMK cells (49,53). These results showed that in both CSM 14.1 and iBMK cells, expression of YFP-Bcl-x_L confers resistance to cell death, thus corroborating the fact that staurosporine triggers death via an apoptosis pathway. Moreover, expression of YFP-Bcl-x_L-ΔTM conferred similar cell death resistance as expression of YFP-Bcl-x_L. We also found, unexpectedly, that expression of YFP-TM confers a moderate level of apoptosis resistance (Fig. 7). Our data suggest that the presence of the BH domains is sufficient for apoptosis resistance and does not require the TM domain or morphological alterations.

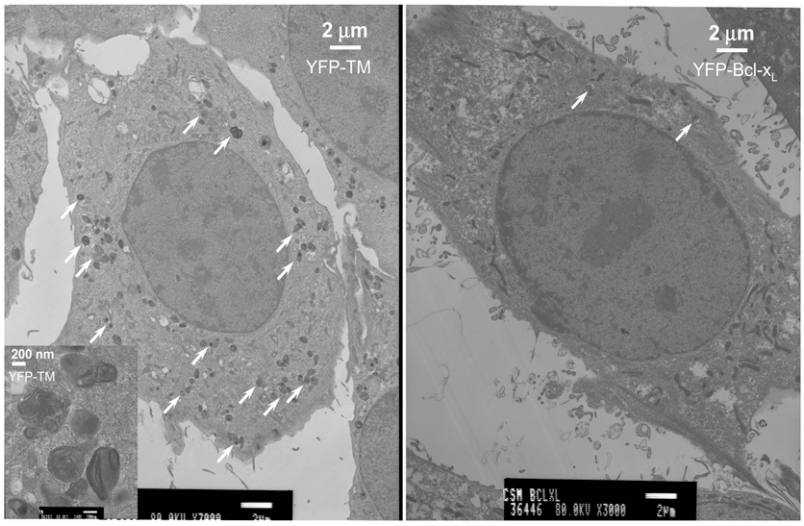

FIGURE 6 Low magnification electron micrographs showing a large number of autophagocytic vesicles (*arrows*) in a representative YFP-TM cell, and comparison with a typical YFP-Bcl-x_L-expressing cell. (*Inset*) High magnification view of a few autophagocytic vesicles in a YFP-TM cell.

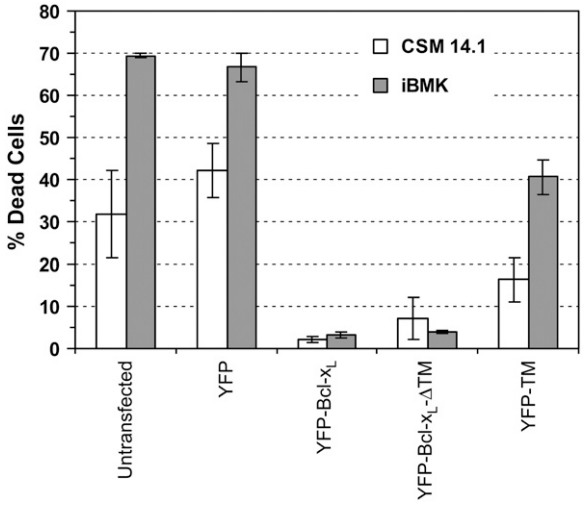

FIGURE 7 Percentage of dead CSM 14.1 and iBMK cells assessed by propidium iodide exclusion after 24 h of treatment with 1 μM staurosporine. Both cell types were stably transfected with YFP, YFP-BCL-x_L, YFP-BCL-x_L-ΔTM, or YFP-TM. Mean $\pm$ SD of at least three cell plates.

This would be possible since, for example, the hydrophobic pocket formed by the BH1-BH3 domains of Bcl-x_L-ΔTM could still sequester BH3-only proteins in the cytoplasm, and in this way inhibit activation of Bax and Bak. Cytoplasmic mutants of Bcl-x_L may also still have minor associations with subcellular membranes and have been reported to retain effective anti-apoptotic activity (17). Certainly, in the case of Bcl-2, a Bcl-2 cytoplasmic mutant lacking the transmembrane domain still possesses anti-apoptotic activity (56), and the viral Bcl-2 homolog E1B19K, which targets organellar membranes by myristoylation, lacks the C-terminal transmembrane domain and inhibits apoptosis by binding Bax or Bak (57). Nevertheless, our results do not exclude the possible secondary role of the TM domain in apoptosis resistance. In particular, the absence of the BH domains in the YFP-TM construct did not fully obliterate the construct's ability to confer apoptosis resistance, and YFP-TM expression did alter mitochondrial morphology. While the mitigating role of autophagy in response to staurosporine-induced cell death in the YFP-TM cells is not clear, the TM domain of Bcl-x_L could still contribute to apoptosis resistance by mediating initial changes in mitochondrial morphology.

In this article, we have used light scattering and electron microscopy to show that the TM domain of Bcl-x_L mediates changes in mitochondrial morphology. The OSIR in our study corresponds to the intensity ratio of wide-to-narrow angle forward scatter, and gives a measure of scattering anisotropy as an estimate of the angular deviation of the scattered light from the forward direction. This ratio decreases monotonically as a function of diameter, D, as shown in Fig. 2 *B*. However, when particles are not spherical, the OSIR can be sensitive to particle shape in addition to particle size, even though it may not be able to distinguish between size and shape alterations (44) . We had also previously shown that for particle geometries approximating mitochondria, varying the refractive index ratio, m, from 1.005 to 1.11 decreases the OSIR by only 1.8% (44). If the refractive index of the cytoplasm is taken as 1.36 corresponding to an equivalent aqueous solution of protein with concentration 15% (15 g/100 ml) (58), changing m from 1.005 to 1.11 is equivalent to changing the protein concentration of the mitochondria from $\sim$20% to $>$90% (58). As such, changes in the refractive index corresponding to extreme changes in particle composition cannot fully account for the measured changes in OSIR for particles the size of mitochondria. We therefore conclude that changes in the OSIR are largely due to changes in particle morphology, rather than composition. One way to interpret the OSIR would be to state that the angular scattering properties of the mitochondria represented by the OSIR are equivalent to the OSIR properties of a sphere of a given size. In this sense, the OSIR decrease measured in this study corresponds to an increase in this ''equivalent scattering diameter.'' However, the relationship between this equivalent diameter and the fine geometrical structure of the mitochondrial matrix is not clear. The expansion of the matrix and reduction in intracristal spaces seen by electron microscopy could correspond to an actual increase in matrix size, or could represent matrix reconfiguration without a significant change in matrix volume. A full three-dimensional characterization of the change in matrix geometry, membrane contact sites, and matrix volume will be necessary to further the electron microscopy and scattering results presented in this study.

Changes in mitochondrial morphology can be produced by several mechanisms, including control of matrix potassium, calcium and ADP content, changes in the configuration of the adenine nucleotide translocase (ANT) and interaction with dynamin-related proteins that normally control mitochondrial fusion and fission. Bcl-2 family proteins have been shown to influence some of these processes. Nonetheless, the transient and steady-state modulation of mitochondrial morphology by Bcl-2 family proteins has not been fully characterized. An increase in mitochondrial volume effected by uptake of K^+ into the matrix has been shown to stimulate respiration (59). However, t-Bid was shown to facilitate cytochrome *c* release by increasing mitochondrial K^+ uptake, while Bcl-2 was shown to inhibit K^+ uptake and cytochrome *c* release, and increase efflux of K^+ from the matrix (31). At the same time, overexpression of Bcl-2 correlated with an increase in mitochondrial matrix volume, but no change in matrix K^+ concentration, and may be related to a greater capacity for calcium uptake into the matrix (60). ADP-induced phosphorylation leads to a change in mitochondrial morphology from the ''orthodox'' to the ''condensed'' configuration, in which the matrix is shrunken with increased intracristal and intermembrane spaces but without an obvious reduction in total mitochondrial volume (34). Conversely, binding of adenine nucleotide to the ANT switches the ANT from its cytosolic to matrix facing conformation and can result in a decrease in intracristal spaces and inner membrane contraction without a

change in matrix volume (61–65). The ANT may be able to influence K^+ influx into the mitochondria (59,66). However, changes in morphology involving the ANT may also be mediated by an alteration of inner/outer membrane contact sites rich in ANT (e.g., ANT-VDAC contact sites) (65,67). In this context, Bcl-x_L was shown to facilitate ADP/ATP exchange across the ANT in response to growth factor withdrawal (27). Consistent with this, Bcl-2 was shown to increase ANT-mediated ADP/ATP exchange, while Bax was shown to decrease it (25). Bax dimers are also thought to facilitate cytochrome *c* release by localizing and interfering with inner/outer membrane contact points involving the ANT (68). Lastly, recent evidence points at the interaction of Bcl-2 family proteins with dynamin-related proteins. Truncated-Bid can disrupt Optic Atrophy 1 oligomers, which control cristae junctions, and was shown to facilitate cytochrome *c* release through a drastic inversion of inner membrane curvature and remodeling of intracristal spaces independently of mitochondrial fusion (20,41). On the other hand, Bax promotes mitochondrial fusion in healthy cells by interacting with mitofusin-2 (22). This interaction may be inhibited during apoptosis and contribute to unbalance Drp-1 induced mitochondrial fragmentation (22). Changes in morphology involving matrix expansion, as observed here, could, for example, precondition mitochondria to counteract death-promoting morphological alterations induced by pro-apoptotic Bcl-2 members, such as truncated-Bid and Bax/Bak. Alternatively, matrix expansion could provide a means to control mitochondrial metabolism and diffusion across mitochondrial membranes by controlling intracristal space and contact points between the inner and outer membranes. While the specific (anti-apoptotic) function of Bcl-x_L that requires localization to the mitochondria and alteration of matrix morphology even before a death stimulus has not been elucidated in this study, our results suggest that the requisite localization of wild-type Bcl-x_L to mitochondria may be necessary for a bioenergetic function mediated by the TM domain and matrix morphology, and distinct from and not requiring BH3 domain sequestration.

We thank Dr. Carmen Mannella for insightful discussion regarding the interpretation of our electron micrographs, Dr. Eileen White for generously providing the iBMK cells and instructive discussions about Bcl-2 family proteins, and Raj Patel of the University of Medicine and Dentistry, New Jersey pathology facility for critical help with the preparation of electron microscopy samples. We also thank Dr. D. E. Bredesen for the original CSM 14.1 cell samples and Dr. Brian Pfister for the YFP and Bcl-x_L CSM14.1 variants.

This work was supported in part by National Institutes of Health grant No. R21RR015264, Biomedical Engineering Research grant No. RG-02-0682 from the Whitaker Foundation, and the Johnson and Johnson Discovery Awards Fund at Rutgers, The State University of New Jersey.

REFERENCES

1. Danial, N. N., and S. J. Korsmeyer. 2004. Cell death: critical control points. *Cell.* 116:205–219.
2. Cory, S., and J. M. Adams. 2002. The BCL2 family: regulators of the cellular life-or-death switch. *Nat. Rev. Cancer.* 2:647–656.
3. Muchmore, S. W., M. Sattler, H. Liang, R. P. Meadows, J. E. Harlan, H. S. Yoon, D. Nettesheim, B. S. Chang, C. B. Thompson, S. L. Wong, S.-C. Ng, and S. W. Fesik. 1996. X-ray and NMR structure of human Bcl-xL, an inhibitor of programmed cell death. *Nature.* 381:335–341.
4. Sattler, M., H. Liang, D. Nettesheim, R. P. Meadows, J. E. Harlan, M. Eberstadt, H. S. Yoon, S. B. Shuker, B. S. Chang, A. J. Minn, C. B. Thompson, and S. W. Fesik. 1997. Structure of BCL-xL-Bak peptide complex: recognition between regulators of apoptosis. *Science.* 275: 983–986.
5. Suzuki, M., R. J. Youle, and N. Tjandra. 2000. Structure of Bax. Coregulation of dimer formation and intracellular localization. *Cell.* 103: 645–654.
6. Jeong, S.-Y., B. Gaume, Y.-J. Lee, Y.-T. Hsu, S.-W. Ryu, S.-H. Yoon, and R. J. Youle. 2004. Bcl-xL sequesters its C-terminal membrane anchor in soluble, cytosolic homodimers. *EMBO J.* 23:2146–2155.
7. Lindsten, T., A. J. Ross, A. King, W.-X. Zong, J. C. Rathmell, H. A. Shiels, E. Ulrich, K. G. Waymire, P. Mahar, K. Frauwirth, Y. Chen, M. Wei, V. M. Eng, D. M. Adelman, M. C. Simon, A. Ma, J. A. Golden, G. Evan, S. J. Korsmeyer, G. R. MacGregor, and C. B. Thompson. 2000. The combined functions of proapoptotic Bcl-2 family members Bak and Bax are essential for normal development of multiple tissues. *Mol. Cell.* 6:1389–1399.
8. Wei, M. C., W.-X. Zong, E. H.-Y. Cheng, T. Lindsten, V. Panoutsakopoulou, A. J. Ross, K. A. Roth, G. R. MacGregor, C. B. Thompson, and S. J. Korsmeyer. 2001. Proapoptotic BAX and BAK: a requisite gateway to mitochondrial dysfunction and death. *Science.* 292:727–730.
9. Cheng, E. H.-Y., M. C. Wei, S. Weiler, R. A. Flavell, T. W. Mak, T. Lindsten, and S. J. Korsmeyer. 2001. BCL-2, BCL-XL sequester BH3 domain-only molecules preventing BAX- and BAK-mediated mitochondrial apoptosis. *Mol. Cell.* 8:705–711.
10. Wei, M. C., T. Lindsten, V. K. Mootha, S. Weiler, A. Gross, M. Ashiya, C. B. Thompson, and S. J. Korsmeyer. 2000. tBid, a membrane-targeted death ligand, oligomerizes BAK to release cytochrome c. *Genes Dev.* 14:2060–2071.
11. Eskes, R., S. Desagher, B. Antonsson, and J.-C. Martinou. 2000. Bid induces the oligomerization and insertion of Bax into the outer mitochondria membrane. *Mol. Cell. Biol.* 20:929–935.
12. Oltvai, Z. N., C. L. Milliman, and S. J. Korsmeyer. 1993. Bcl-2 heterodimerizes in vivo with a conserved homolog, Bax, that accelerates programmed cell death. *Cell.* 74:609–619.
13. Yin, X.-M., Z. N. Oltvai, and S. J. Korsmeyer. 1994. BH1 and BH2 domains of Bcl-2 are required for inhibition of apoptosis and heterodimerization with Bax. *Nature.* 369:321–323.
14. Cuconati, A., C. Mukherjee, D. Perez, and E. White. 2003. DNA damage response and MCL-1 destruction initiate apoptosis in adenovirus-infected cells. *Genes Dev.* 17:2922–2932.
15. Willis, S. N., L. Chen, G. Dewson, A. Wei, E. Naik, J. I. Fletcher, J. M. Adams, and D. C. S. Huang. 2005. Proapoptotic Bak is sequestered by Mcl-1 and Bcl-xL, but not Bcl-2, until displaced by BH3-only proteins. *Genes Dev.* 19:1294–1305.
16. Gonzalez-Garcia, M., R. Perez-Ballestero, L. Ding, L. Duan, L. H. Boise, C. B. Thompson, and D. Nunez. 1994. Bcl-xL is the major Bcl-x mRNA form expressed during murine development and its product localizes to mitochondria. *Development.* 120:3033–3042.
17. Kaufmann, T., S. Schlipf, J. Sanz, K. Neubert, R. Stein, and C. Borner. 2003. Characterization of the signal that directs Bcl-xL, but not Bcl-2, to the mitochondrial outer membrane. *J. Cell Biol.* 160:53–64.
18. Hsu, Y.-T., K. G. Wolter, and R. J. Youle. 1997. Cytosol-to-membrane redistribution of Bax and Bcl-X_L during apoptosis. *Proc. Natl. Acad. Sci. USA.* 94:3668–3672.
19. Cuttle, L., X.-J. Zhang, Z. H. Endre, C. Winterford, and G. C. Gobe. 2001. Bcl-X_L translocation in renal tubular epithelial cells in vitro protects distal cells from oxidative stress. *Kidney Int.* 59:1779–1788.
20. Scorrano, L., M. Ashiya, K. Buttle, S. Weiler, S. A. Oakes, C. A. Mannella, and S. J. Korsmeyer. 2002. A distinct pathway remodels

mitochondrial cristae and mobilizes cytochrome *c* during apoptosis. *Dev. Cell.* 2:55–67.

21. Gonzalvez, F., F. Pariselli, P. Dupaigne, I. Budihardjo, M. Lutter, B. Antonsson, P. Diolez, S. Manon, J.-C. Martinou, M. Goubern, X. Wang, S. Bernard, and P. X. Petit. 2005. tBid interaction with cardiolipin primarily orchestrates mitochondrial dysfunctions and subsequently activates Bax and Bak. *Cell Death Differ.* 12:614–626.
22. Karbowski, M., K. L. Norris, M. M. Cleland, S.-Y. Jeong, and R. J. Youle. 2006. Role of Bax and Bak in mitochondrial morphogenesis. *Nature.* 443:658–662.
23. Shimizu, S., M. Narita, and Y. Tsujimoto. 1999. Bcl-2 family proteins regulate the release of apoptogenic cytochrome *c* by the mitochondrial channel VDAC. *Nature.* 399:383–387.
24. Cheng, E. H.-Y., T. V. Sheiko, J. K. Fisher, W. J. Craigen, and S. J. Korsmeyer. 2003. VDAC2 inhibits BAK activation and mitochondrial apoptosis. *Science.* 301:513–517.
25. Belzacq, A.-S., H. L. A. Vieira, F. Verrier, G. Vandecasteele, I. Cohen, M.-C. Prevost, E. Larquet, F. Pariselli, P. X. Petit, A. Kahn, and R. Rizzuto. 2003. Bcl-2 and Bax modulate adenine nucleotide translocase activity. *Cancer Res.* 63:541–546.
26. Vander-Heiden, M. G., N. S. Chandel, E. K. Williamson, P. T. Schumacker, and C. B. Thompson. 1997. Bcl-xL regulates the membrane potential and volume homeostasis of mitochondria. *Cell.* 91:627–637.
27. Vander-Heiden, M. G., N. S. Chandel, P. T. Schumacker, and C. B. Thompson. 1999. Bcl-xL prevents cell death following growth factor withdrawal by facilitating mitochondrial ATP/ADP exchange. *Mol. Cell.* 3:159–167.
28. Vander-Heiden, M. G., X. X. Li, E. Gottlieb, R. B. Hill, C. B. Thompson, and M. Colombini. 2001. Bcl-xL promotes the open configuration of the voltage-dependent anion channel and metabolite passage through the outer mitochondrial membrane. *J. Biol. Chem.* 276:19414–19419.
29. Gottlieb, E., M. G. V. Heiden, and C. B. Thompson. 2000. Bcl-xL prevents the initial decrease in mitochondrial membrane potential and subsequent reactive oxygen species production during tumor necrosis α-induced apoptosis. *Mol. Cell. Biol.* 20:5680–5689.
30. Kowaltowski, A. J., A. E. Vercesi, and G. Fiskum. 2000. Bcl-2 prevents mitochondrial permeability transition and cytochrome *c* release via maintenance of reduced pyridine nucleotides. *Cell Death Differ.* 7:903–910.
31. Eliseev, R. A., J. D. Salter, K. K. Gunter, and T. E. Gunter. 2003. Bcl-2 and tBid proteins counter-regulate mitochondrial potassium transport. *Biochim. Biophys. Acta.* 1604:1–5.
32. Lehninger, A. L. 1959. Reversal of thyroxine-induced swelling of rat liver mitochondria by adenosine triphosphate. *J. Biol. Chem.* 234:2187–2195.
33. Packer, L. 1960. Metabolic and structural states of mitochondria. *J. Biol. Chem.* 235:242–249.
34. Hackenbrock, C. R. 1966. Ultrastructural bases for metabolically linked mechanical activity in mitochondria I. *J. Cell Biol.* 30:269–297.
35. Packer, L. 1967. Energy-linked low amplitude mitochondrial swelling. *In* Methods in Enzymology, Vol. 10. R. W. Estabrook and M. E. Pullman, editors. Academic Press, New York.
36. Harris, R. A., M. A. Asbell, J. Asai, W. W. Jolly, and D. E. Green. 1969. The conformational basis of energy transduction in membrane systems. V. Measurement of configurational changes by light scattering. *Arch. Biochem. Biophys.* 132:545–560.
37. Hunter, D. R., R. A. Haworth, and J. H. Southward. 1976. Relationship between configuration, function, and permeability in calcium-treated mitochondria. *J. Biol. Chem.* 251:5069–5077.
38. Olichon, A., L. Baricault, N. Gas, E. Guillou, A. Valette, P. Belenguer, and G. Lenaers. 2003. Loss of OPA1 perturbates the mitochondrial inner membrane structure and integrity, leading to cytochrome *c* release and apoptosis. *J. Biol. Chem.* 278:7743–7746.
39. Mannella, C. A. 2006. The relevance of mitochondrial membrane topology to mitochondrial function. *Biochim. Biophys. Acta.* 1762:140–147.
40. Cipolat, S., T. Rudka, D. Hartmann, V. Costa, L. Serneels, K. Craessaerts, K. Metzger, C. Frezza, W. Annaert, L. D'Adamio, C. Derks, R. Dejaegere, L. Pellegrini, R. D'Hooge, L. Scorrano, and B. DeStrooper. 2006. Mitochondrial rhomboid PARL regulates cytochrome *c* release during apoptosis via OPA1-dependent cristae remodeling. *Cell.* 126:163–175.
41. Frezza, C., S. Cipolat, O. M. D. Brito, M. Micaroni, G. V. Beznoussenko, T. Rudka, D. Bartoli, R. S. Polishuck, N. N. Danial, B. DeStrooper, and L. Scorrano. 2006. OPA1 controls apoptotic cristae remodeling independently from mitochondrial fusion. *Cell.* 126:177–189.
42. Mannella, C. A. 2006. Structure and dynamics of the mitochondrial inner membrane cristae. *Biochim. Biophys. Acta.* 1763:542–548.
43. Quinlan, P. T., A. P. Thomas, A. E. Armston, and A. P. Halestrap. 1983. Measurement of intramitochondrial volume in hepatocytes without cell disruption and its elevation by hormones and valinomycin. *Biochem. J.* 214:395–404.
44. Boustany, N. N., R. Drezek, and N. V. Thakor. 2002. Calcium-induced alterations in mitochondrial morphology quantified in situ with optical scatter imaging. *Biophys. J.* 83:1691–1700.
45. Wilson, J. D., C. E. Bigelow, D. J. Calkins, and T. H. Foster. 2005. Light scattering from intact cells reports oxidative-stress-induced mitochondrial swelling. *Biophys. J.* 88:2929–2938.
46. Shuele, G., E. Vitkin, P. Huie, C. O'Connell-Rodwell, D. Palanker, and L. T. Perelman. 2005. Optical spectroscopy noninvasively monitors response of organelles to cellular stress. *J. Biomed. Opt.* 10: 051404.
47. Beauvoit, B., and B. Chance. 1998. Time-resolved spectroscopy of mitochondria, cells and tissues under normal and pathological conditions. *Mol. Cell. Biochem.* 184:445–455.
48. Johnson, L. J., W. Chung, D. F. Hanley, and N. V. Thakor. 2002. Optical scatter imaging detects mitochondrial swelling in living tissue slices. *Neuroimage.* 17:1649–1657.
49. Boustany, N. N., Y. C. Tsai, B. Pfister, W. M. Joiner, G. A. Oyler, and N. V. Thakor. 2004. BCL-x(L)-dependent light scattering by apoptotic cells. *Biophys. J.* 87:4163–4171.
50. Boustany, N. N., S. C. Kuo, and N. V. Thakor. 2001. Optical scatter imaging: subcellular morphometry in situ with Fourier filtering. *Opt. Lett.* 26:1063–1065.
51. Astola, J., and P. Kuosmanen. 1997. Fundamentals of Nonlinear Digital Filtering. CRC Press, Boca Raton, FL.
52. Vernon, D. 1991. Machine Vision. Prentice-Hall, Englewood Cliffs, NJ.
53. Degenhardt, K., G. Chen, T. Lindsten, and E. White. 2002. Bax and Bak mediate p53-independent suppression of tumorigenesis. *Cancer Cell.* 2:193–203.
54. Oberstein, A., P. D. Jeffrey, and Y. Shi. 2007. Crystal structure of the Bcl-xL-Beclin 1 peptide complex, Beclin 1 is a novel BH3-only protein. *J. Biol. Chem.* 282:13123–13132.
55. Chiara-Maiuri, M., G. LeToumelin, A. Criollo, J.-C. Rain, F. Gautier, P. Juin, E. Tasdemir, G. Pierron, K. Troulinaki, N. Tavernarakis, J. A. Hickman, O. Geneste, and G. Kroemer. 2007. Functional and physical interaction between Bcl-xL and the BH3-like domain in Beclin-1. *EMBO J.* (April):19 (Epub ahead of print.).
56. Borner, C., I. Martinou, C. Mattmann, M. Irmler, E. Schaerer, J.-C. Martinou, and J. Tschopp. 1994. The protein bcl-2α does not require membrane attachment, but two conserved domains to suppress apoptosis. *j. cell biol.* 126:1059–1068.
57. Cuconati, A., and E. White. 2002. Viral homologs of BCL-2: role of apoptosis in the regulation of virus infection. *Genes Dev.* 16:2465–2478.
58. Barer, R. 1957. Refractometry and interferometry of living cells. *J. Opt. Soc. Am.* 47:545–556.
59. Halestrap, A. P. 1989. The regulation of the matrix volume of mammalian mitochondria in vivo and in vitro and its role in the control of mitochondrial metabolism. *Biochim. Biophys. Acta.* 973:355–382.
60. Kowaltowski, A. J., R. G. Cosso, C. B. Campos, and G. Fiskum. 2002. Effect of Bcl-2 overexpression on mitochondrial structure and function. *J. Biol. Chem.* 277:42802–42807.

61. Stoner, C. D., and H. D. Sirak. 1973. Adenine nucleotide-induced contraction of the inner mitochondrial membrane. 1. General characterization. *J. Cell Biol.* 56:51–64.

62. Stoner, C. D., and H. D. Sirak. 1973. Adenine nucleotide-induced contraction of the inner mitochondrial membrane, 2. Effect of bongkrekic acid. *J. Cell Biol.* 56:65–73.

63. Klingenberg, M., K. Grebe, and B. Scherer. 1971. Opposite effects of bongkrekic acid and atractyloside on the adenine nucleotides induced mitochondrial volume changes and on the efflux of adenine nucleotides. *FEBS Lett.* 16:253–256.

64. Klingenberg, M. 1980. The ADP-ATP translocation in mitochondria, a membrane potential controlled transport. *J. Membr. Biol.* 56:97–105.

65. Das, M., J. E. Parker, and A. P. Halestrap. 2003. Matrix volume measurements challenge the existence of diazoxide/glibencamide-sensitive K-ATP channels in rat mitochondria. *J. Physiol. (Lond.).* 547:893–902.

66. Brustovetsky, T., N. Shalbuyeva, and N. Brustovetsky. 2005. Lack of manifestations of diazoxide/5-hydroxydecanoate-sensitive KATP channel in rat brain nonsynaptosomal mitochondria. *J. Physiol. (Lond.).* 568:47–59.

67. Beavis, A. D., R. D. Brannan, and K. D. Garlid. 1985. Swelling and contraction of the mitochondrial matrix. *J. Biol. Chem.* 260:13424–13433.

68. Doran, E., and A. P. Halestrap. 2000. Cytochrome *c* release from isolated rat liver mitochondria can occur independently of outer-membrane rupture: possible role of contact sites. *Biochem. J.* 348:343–350.